Tellus (1999), 51A, 815–832
Printed in UK – all rights reserved

TELLUS
ISSN 0280–6495

The response of atmospheric heat transport to zonally-averaged SST trends

By GUDRUN MAGNUSDOTTIR[1]* and R. SARAVANAN[2], [1]*Department of Earth System Science, University of California, Irvine, California 92697-3100, USA and* [2]*National Center for Atmospheric Research,*† *Boulder, Colorado 80307-3000, USA*

(Manuscript received 14 September 1998; in final form 11 February 1999)

ABSTRACT

We compute the atmospheric heat transport in a realistic atmospheric general circulation model under five different configurations of implied heat transport in the ocean. The implied oceanic heat transport is varied by changing the meridional gradient of sea surface temperature (SST). Climatological SSTs are employed for the control run. The other runs differ in that a zonally symmetric component is added to or subtracted from the climatological SST field. The meridional structure of the variation in SST gradient is based on the observed change in zonally averaged SST over the last century. The SST trend has maxima of about 1 K at high latitudes of both hemispheres. Elsewhere, the change in SST over the last century is fairly uniform at about 0.5 K. We find that in the annual mean, the atmosphere adjusts so that the total meridional heat transport (by atmosphere and ocean) is rather insensitive to the change in zonally averaged SST. Interannual variability in the annual mean heat transport is minor in each of these cases. There is a large degree of compensation even between the different components of atmospheric heat transport such that changes in latent heat transport usually go hand in hand with changes in dry static energy transport of an opposite sign. The radiative flux at the top of the atmosphere is affected the most by the change in SST in the tropics, where the shortwave component shows a strong negative feedback and the longwave component shows a weak positive feedback. Concentrating on the winter season in the Northern Hemisphere, we find that when we decrease the meridional SST gradient (i.e., warm the sea surface at high latitudes the most), the stationary waves accomplish more of the poleward heat transport than before. When we increase the meridional SST gradient, the heat flux due to both transient and stationary waves increases, although not by nearly as much as most eddy parameterization schemes would predict. The winter season in the Southern Hemisphere shows a substantial increase in heat transport by transient waves when the meridional SST gradient is increased. Their maximum heat transport is greater and extends over a wider band of latitudes than in the control case. Because the Southern Hemisphere is mostly covered by ocean, the stationary waves are weak and play a minor rôle in atmospheric heat transport.

1. Introduction

The climate system acts as a "heat engine" that transports heat from the warm equator to the cold poles. The two fluid components of the climate system, the atmosphere and the ocean, both contribute significantly to this meridional heat transport. Baroclinic processes in the atmosphere, such as the Hadley circulation, and extratropical transient/stationary waves, play a crucial rôle in transporting heat meridionally, as does the thermohaline circulation in the ocean. The meridional heat transport is therefore an important measure of the climatic state. In this study, we focus on

* Corresponding author. e-mail: gudrun@uci.edu.
† The National Center for Atmospheric Research is sponsored by the National Science Foundation.

the atmospheric component of this meridional heat transport, and analyze its relationship with the meridional gradient of the sea surface temperature (SST). Some of the issues that we address are the degree to which changes in the (implied) oceanic meridional heat transport are compensated by different atmospheric processes, and also the rôle of variations in top-of-the-atmosphere radiative balance.

The partitioning of the total poleward heat transport between the atmosphere and the ocean has to be considered an issue of great significance for understanding and modelling climate variations. For building climate models that couple the circulation of the atmosphere to that of the ocean, it is essential to have an accurate representation of this partitioning in order to avoid the unrealistic flux adjustments that many past coupled models have required (Kerr, 1995). It is well established that the highly nonlinear nature of the oceanic thermohaline circulation allows for multiple equilibria (e.g., Stommel, 1961; Bryan, 1986; Manabe and Stouffer, 1988). Each of these different states of the thermohaline circulation corresponds to a widely different poleward heat transport in the ocean. Various paleoclimatic data show evidence for significant decadal scale variability in the North Atlantic region during the last glacial maximum (Broecker et al., 1985). The fact that evidence of these climate variations is only found in Europe, Greenland and the Newfoundland area of North America and not elsewhere on the American continent, suggests that they may be linked to variations in the thermohaline circulation. Even if we are not considering climate states as widely different as those corresponding to a present-day thermohaline circulation versus a state without any North Atlantic deep water formation, a compelling question to ask is the following: How will the atmospheric heat transport respond to a changed ocean heat transport?

Using very simple energy-balance arguments, Stone (1978) deduced that the total annual meridional heat transport of the combined ocean–atmosphere system appears to be remarkably insensitive to the details of its different contributions. He attributed this insensitivity to two different effects. Firstly, at the top of the atmosphere there is considerable correlation between the local absorbed shortwave radiation (ASR) and the local outgoing longwave radiation (OLR). This is the well known effect of relating a high (local) planetary albedo to a low (local) planetary temperature and hence low thermal emission. Secondly, the high efficiency of dynamical transport mechanisms in the atmosphere contributes to the near constancy of the total annual meridional heat transport.

North (1975) found that for a zonally averaged, annual-mean, energy-balance model, where the meridional heat transport is modelled by thermal diffusion, only two modes of the expansion of variables in terms of Legendre polynomials are required for adequate representation. In fact, Budyko's (1969) purely empirical model is obtained from this two-mode model if the thermal diffusion coefficient is assumed to be constant. In the context of one-dimensional, heat-balance climate models, the dynamical efficiency may be thought of as this horizontal diffusion coefficient. Rahmstorf and Willebrand (1995) explore the high dynamical efficiency of the atmosphere in setting boundary conditions for an ocean climate model. Usually such models have been forced by a constant atmospheric temperature implying that the atmosphere has infinite heat capacity, which is highly unrealistic for the purpose of studying climate variability. When a representation of the atmospheric dynamical efficiency (in the form of diffusive horizontal transport) is included in the boundary conditions, the thermohaline circulation becomes more stable to small perturbations.

Green (1970) approached the problem of determining heat transport by atmospheric eddies by the concept of diffusion. Several papers by Stone and collaborators have discussed ways of parameterising the atmospheric eddy heat transport (T_{A_e}) in terms of the low-level meridional temperature gradient (δT). Usually a relation of the following form is assumed, $T_{A_e} \propto (\delta T)^n$, where n is a constant to be determined. (Note that for the two-mode, energy-balance models with a constant thermal diffusion coefficient discussed above, $n = 1$.) Stone and Miller (1980) looked at the seasonal cycle to relate atmospheric eddy transport to the 1000 mb meridional temperature gradient. In their empirical study they arrive at the value of $n = 2$ in the above relation. A drawback on the validity of their study is the fact that the mean climate state changes significantly as the system goes through the annual cycle. Other stud-

ies using two-layer atmospheric models of varying complexities have arrived at numbers ranging from $n = 15$ in a quasi-geostrophic model (Stone and Branscome, 1992), to $n = 6$ in a balanced model on the sphere with fixed static stability (Zhou and Stone, 1993a), to $n = 3$ in a balanced model on the sphere where static stability is allowed to vary (Zhou and Stone, 1993b).

It is of interest that in their data analysis, Stone and Miller (1980) find that there is a negative feedback between the transient and stationary eddy fluxes of heat in the atmosphere. Manabe and Bryan (1985) find in a coupled general circulation model study of changing concentration of CO_2 that the total heat transport in the atmosphere–ocean system is nearly constant thus confirming Stone's (1978) result. Moreover, the thermohaline circulation is almost unchanged between experiments, which involve as much as an eightfold increase in CO_2, so that the compensation in heat transport is occurring within the atmosphere. They find that there is a strong negative feedback between the latent heat transport and the dry static energy transport. Saravanan and McWilliams (1995) find in an intermediate coupled model that the total poleward heat transport tends to remain nearly constant under widely different climate scenarios. This implies that in their relatively simple coupled model, the eddy-resolving atmosphere tends to make up for differences in the oceanic heat transport, even when they involve a halocline catastrophe. It has not yet been determined if this is the case for Earth's climate, or even if this holds true in the more sophisticated coupled climate models.

Trenberth and Solomon (1994) used ECMWF atmospheric analysis for 1988 to compute the local monthly atmospheric heat budget. When combined with radiation data from the Earth Radiation Budget Experiment (ERBE) satellites for the same year, the implied ocean transport could be computed as a residual. This was the last year for which reliable data could be obtained from ERBE. At the same time considerable improvements had been made in atmospheric analysis, especially in representing the low-latitude divergent circulations. Thus their profile of the implied oceanic heat transport is considered more reliable than earlier estimates that rely on atmospheric radiosonde data (e.g., Carissimo et al., 1985, and references therein). Keith (1995) computed heat transport of the atmosphere and ocean based on ERBE radiation measurements and both ECMWF and NMC atmospheric analysis for various years to form a very comprehensive analysis of the zonally averaged budgets for the annual and seasonal average. He found that interannual variability is negligible and that overall the more recent atmospheric datasets from both centres show remarkable agreement. Zhang and Rossow (1997) used the four-year International Cloud Climatology Project dataset to compute meridional heat transports in the atmosphere and ocean based on the total vertical energy fluxes at the top of the atmosphere and at the surface. Despite uncertainties in determining surface energy fluxes, their results indicate a general agreement with earlier results.

Even if we had reliable atmospheric analysis combined with satellite data of the top-of-atmosphere radiation budget for longer periods of time than a few years, it is doubtful whether the climate signal in terms of changes in the meridional heat budget would be detectable. Thus carefully planned numerical experiments using sophisticated climate models seem to be most promising. Rather than turning to a sophisticated *coupled* climate model, which is very expensive to run, here we take the frugal approach to obtaining answers. Since we are primarily interested in the atmospheric response, we run a realistic atmospheric general circulation model (GCM), the NCAR CCM3 with fixed SSTs. In order to represent different configurations of the poleward (implied) oceanic heat transport, we vary the meridional gradient of SST. Not having to represent the oceanic circulation coupled to that of the atmosphere saves enormous computer time, a fraction of which can in turn be used to explore the parameter space of different SST distributions.

Natural and anthropogenic climate variations could both lead to changes in the meridional heat transport in the ocean, which would be reflected in changes in the SST distribution. Rather than trying to distinguish between these two different effects, we simply use the observed changes in SST over the past century to define a characteristic latitudinal profile of SST variability. Different amplitudes of this zonally uniform characteristic SST variability pattern are added to (or subtracted from) the climatological SST distribution to gener-

ate different scenarios of global SST variability. Each of these SST scenarios will, of course, correspond to a different implied oceanic heat transport. Five such SST scenarios are used as surface boundary conditions to force the atmospheric GCM.

In this paper the emphasis is on the response of the vertically integrated, atmospheric meridional heat transport and its various decompositions. We also examine the closely-related quantities of vertical energy fluxes at both boundaries. Section 2 describes the model and data, and details of the numerical experiments. It also contains a brief discussion of atmospheric energetics. Section 3 contains results for the annual-mean meridional heat budget and boundary energy fluxes. We discuss results for the control simulation (of climatological SST) and examine the response of the other cases as deviations from the control. In particular, we examine the latent heat transport and dry static energy transport separately. Section 4 contains results for the winter season of each hemisphere. In addition to looking at contributions of dry static energy and latent heat to the atmospheric transport, we also separate the heat transport into portions due to transient and stationary eddies. Section 5 contains a discussion of how our results compare with some earlier ideas of heat flux parameterisation as well as a summary and conclusions.

2. Some preliminaries

2.1. Model and SSTs

The numerical experiments were run with the NCAR Community Climate Model, CCM3 (Kiehl et al., 1998a). The horizontal resolution was T42 (equivalent to 2.8° lat × 2.8° long) with 18 vertical layers, which is a standard configuration. The boundary forcing is specified in the form of monthly mean SSTs that are interpolated linearly in time between months. The different experiments differ only in the SST field that is specified for each case. Each experiment was run for 10 years. In what follows, $0X$ is the name of the experiment that is forced by the climatological SST field.

To retain a degree of realism, we varied the meridional SST gradient such that the spatial structure of the variation agrees with the centennial trend in observations. The dashed curve in Fig. 1 shows the least-square trend in the zonally and annually averaged GISST2 data (Rayner et al., 1995). The solid curve shows this same field after applying spatial smoothing where we interpolate the data using the first 15 Legendre poynomials. The data set extends over almost the entire last century or from 1903 to 1994. The trend in Fig. 1 is expressed in K per century. Even after the smoothing there is a very clear meridional structure to the trend, consisting of a strong signal of almost 1 K per century at high latitudes in both hemispheres. This was the structure by which the SST was varied in the different experiments.

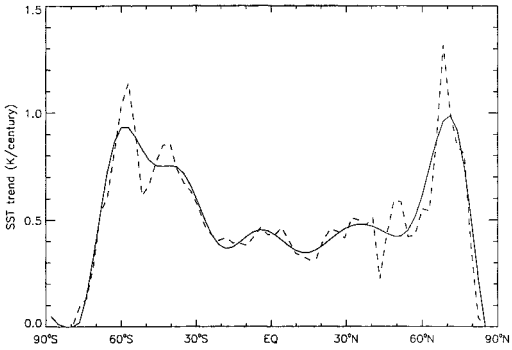

Fig. 1. Least-square trend in annual-mean, zonally averaged sea surface temperature (in K per century) from GISST2 data as a function of latitude. The dashed curve represents the raw data. The solid curve represents the data after spatial smoothing.

Table 1 gives an overview of the numerical experiments. We use the term "trend-factor" to refer to the factor by which the centennial trend in zonally averaged SSTs is multiplied in each experiment. We add the spatially smoothed centennial trend described above to the climatological SST field for each month (SST_{clim}) when forcing $1X$. We add five times the centennial trend to SST_{clim} when forcing $5X$. We subtract five times the centennial trend from SST_{clim} when forcing $-5X$. We add nine times the centennial trend to SST_{clim} when forcing $9X$. The change in globally averaged mean surface temperature for all of these experiments was within the range of values usually obtained in global change scenarios.

Note that sea ice is not predicted in CCM3, rather it is prescribed. The atmospheric model assumes that ice forms at the sea surface when the SST value drops below -1.8°C in the control experiment ($0X$), thus modifying surface properties such as albedo. We use the same criterion in

Table 1. *The different numerical experiments and the associated trend-factor (first column) indicating the imposed SST (second column) and the resulting change in globally averaged surface temperature (third column, in K) from the control (0X): the fourth column shows the resulting change in average surface temperature (in K) over land only*

Experiment (trend-factor)	SST	ΔT_{sfc}, K (global)	ΔT_{sfc}, K (only over land)
$0X$	$SST_{clim}(\lambda, \phi)$	0	0
$1X$	$SST_{clim}(\lambda, \phi) + trend(\phi)$	1.5	1.5
$5X$	$SST_{clim}(\lambda, \phi) + 5 \cdot trend(\phi)$	3.7	4.0
$-5X$	$SST_{clim}(\lambda, \phi) - 5 \cdot trend(\phi)$	−3.2	−3.0
$9X$	$SST_{clim}(\lambda, \phi) + 9 \cdot trend(\phi)$	5.9	6.4

the perturbation experiments. This means that the sea-ice extent is different for the different experiments. To compare the extent of sea ice for the various experiments, we calculated the area covered by sea ice in the annual mean as a function of latitude. The results are shown in Fig. 2 as the fraction of sea-surface area that is ice-covered as a function of latitude. The solid curve represents $0X$, the dotted curve $-5X$, the remaining cases, $1X$, $5X$ and $9X$, all have virtually no sea ice, as shown by the dashed curve. Since the variation in sea ice coverage for the different cases is quite arbitrary, we shall confine our analysis mostly to the low and middle latitudes, which are not directly affected by sea ice.

In each of these experiments, the composition of the atmosphere is kept at present day values. In the past, considerable attention has been paid to GCM experiments with double the concentration of carbon dioxide. Such experiments (atmosphere and mixed-layer ocean) predict a rise in the globally averaged surface temperature of anywhere from 2 K to 5 K depending on the GCM (e.g., IPCC, 1996). To place the current experiments in the context of global-change type experiments, we calculated the globally averaged, surface temperature change in each case. For the control case, $0X$, this temperature is 14.3°C. The change in globally averaged temperature from the control is shown in the third column of Table 1. Our $5X$ and $9X$ experiments fall within the the range of typical global-change type experiments, being associated with global average surface temperature increases of the order of 3–6 K. The last column in Table 1 shows the over-land-only average change in surface temperature. In all cases the change in average surface temperature over land was at least as large as the change in the global-mean temperature.

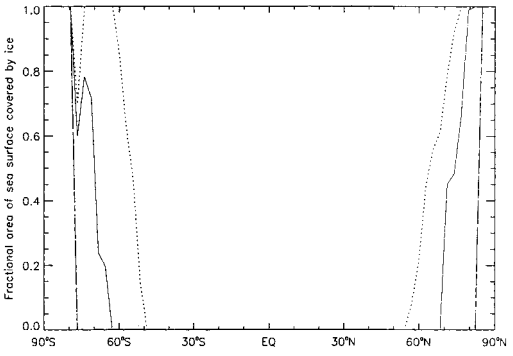

Fig. 2. Fractional area of the ocean surface that is covered by sea ice in the annual mean as a function of latitude. $0X$ (solid); $-5X$ (dotted); $1X$, $5X$ and $9X$ (dashed).

2.2. *The atmospheric energy budget*

In our analysis we use the hybrid vertical coordinate, η, which is the vertical coordinate in the model (Kiehl et al., 1996) and is equivalent to sigma at lower levels and normalized pressure higher up. Following Kasahara (1974), the energy equation can be expressed as

$$\begin{aligned}
&\frac{\partial}{\partial t}\{(c_p T + Lq + \tfrac{1}{2}\boldsymbol{v}\cdot\boldsymbol{v})\tilde{\rho}\} \\
&\quad + \nabla\cdot\{(c_p T + gz + Lq + \tfrac{1}{2}\boldsymbol{v}\cdot\boldsymbol{v})\boldsymbol{v}\tilde{\rho}\} \\
&\quad + \frac{\partial}{\partial \eta}\{(c_p T + gz + Lq + \tfrac{1}{2}\boldsymbol{v}\cdot\boldsymbol{v})\dot{\eta}\tilde{\rho}\} \\
&\quad = \frac{\partial}{\partial \eta}\left(z\frac{\partial p}{\partial t}\right) + \tilde{\rho}(Q_1 - Q_2 + \boldsymbol{v}\cdot\boldsymbol{F}),
\end{aligned} \tag{2.1}$$

where $\tilde{\rho}$ is the mass density in η coordinates, $\boldsymbol{v}$ the horizontal velocity on η surfaces, $\dot{\eta}$ the vertical velocity, $D = \tilde{\rho}(Q_1 - Q_2 + \boldsymbol{v} \cdot \boldsymbol{F})$ represents diabatic terms corresponding to sensible, latent and frictional heating, respectively. Other notation is standard. Hereafter we shall neglect kinetic energy density, which is approximately three orders of magnitude smaller than the other terms. For future reference, moist static energy density is the sum of dry static energy density ($c_p T + gz$) and the latent heat density (Lq).

If we integrate (2.1) in the vertical from $\eta = 1$ to $\eta = 0$, we obtain

$$\frac{\partial}{\partial t}\int_1^0 (c_p T + Lq)\tilde{\rho}\,\mathrm{d}\eta + \nabla\cdot\int_1^0 (c_p T + gz + Lq)\boldsymbol{v}\tilde{\rho}\,\mathrm{d}\eta = z_{\mathrm{sfc}}\frac{\partial p_{\mathrm{sfc}}}{\partial t} + \int_1^0 D\,\mathrm{d}\eta, \tag{2.2}$$

where z_{sfc} is the height of the surface topography and p_{sfc} is the surface pressure. After taking a zonal average of (2.2) only the latitudinal derivative of the divergence term is left. We shall note zonal averages by square brackets $[(\cdot)]$ and time averages by an overbar $\overline{(\cdot)}$. Taking a zonal average of (2.2) and a time mean over a year, we obtain

$$\frac{\partial \cos\phi}{a\cos\phi\,\partial\phi}\overline{[T_{\mathrm{A}}]} \equiv \frac{\partial \cos\phi}{a\cos\phi\,\partial\phi}\overline{\left[\int_1^0 (c_p T + gz + Lq)v\tilde{\rho}\,\mathrm{d}\eta\right]} = \overline{[-F_T - F_S + \mathrm{SHF} + \mathrm{LHF}]}, \tag{2.3}$$

where T_{A} denotes the vertically integrated atmospheric heat flux. Note that we have neglected the storage term in the annual average. Over the course of a year, the time rate of change of atmospheric energy density is much less than the mean net heating rate. We have also neglected the annual average of surface pressure tendency. The terms on the right hand side of (2.3) represent fluxes of energy out of the atmosphere at the top of the atmosphere and at the surface. F_{T} represents the net upward flux of radiation at the top of the atmosphere, or the outgoing longwave radiation (OLR) minus the absorbed solar radiation (ASR), such that $F_{\mathrm{T}} = \mathrm{OLR} - \mathrm{ASR}$. F_{S} represents the net downward flux of radiation at the surface, such that $F_{\mathrm{S}} = \mathrm{LWF} + \mathrm{SWF}$ where LWF refers to net downward longwave radiation and SWF refers to net downward shortwave radiation. LHF and SHF represent the flux of latent and sensible heat at the surface (positive into the atmosphere). Thus the net downward surface heat flux is equal to $F_{\mathrm{S}} - \mathrm{LHF} - \mathrm{SHF}$. In order for this method of evaluating the meridional heat flux to work, the global average flux into the system must equal zero. We therefore subtract the annual global average flux from the right hand side. In any event, the model is tuned so that this quantity is small for current climate (Kiehl et al., 1998b, hereafter KHH). For our experiments this residual term has the following values: For $0X$, it is 0.2 W m^{-2}, for $1X$ it is 0.7 W m^{-2}, for $5X$ it is -3 W m^{-2}, for $-5X$ it is 3 W m^{-2}, for $9X$ it is -6 W m^{-2}.

The frictional heating term, $\boldsymbol{v} \cdot \boldsymbol{F}$, is included in the temperature tendency equation of CCM3 (KHH). Thus the boundary-flux approach to estimating heat transports (right-hand side of (2.3)) will give the right answer. The explicit transport (left-hand side of (2.3)) will be slightly in error because we have not included frictional heating. This will unavoidably lead to inconsistencies when evaluating heat transports using both methods. In general, for annual mean budgets it is more accurate to use the boundary fluxes to evaluate the vertically integrated heat transport. For shorter time periods, e.g., a seasonal mean, the storage terms may be evaluated and one can still use the boundary fluxes. If one wishes to separate the heat transport into components corresponding to transient and standing eddies, and the mean meridional circulation, one must evaluate the transport from model data in the atmosphere. The same goes for separating the heat transport into components of dry static energy and latent heat. In these cases, one cannot include the effects of model frictional heating and diffusion when calculating the meridional heat transport.

Similar arguments may be used for evaluating the vertically integrated meridional heat transport in the combined atmosphere–ocean system (the fluid components of the climate system) in the annual mean. In that case, we obtain

$$\frac{\partial \cos\phi}{a\cos\phi\,\partial\phi}\overline{[T_{\mathrm{A+O}}]} = \overline{[-F_{\mathrm{T}}]}. \tag{2.4}$$

The implied oceanic heat transport may then be obtained by subtracting (2.3) from (2.4) and we find that the divergence of the annual mean,

implied oceanic heat transport is simply equal to the annual mean net surface energy flux.

3. Annual-mean budgets

3.1. Meridional budgets of CCM3 for current climate

The latest version of the Community Climate Model presents major improvements over earlier versions especially in terms of the surface energy budget and the hydrological cycle. KHH present a comprehensive study of the simulated energy budget of CCM3 based on a 15 year integration using observed monthly mean SSTs from 1979–1993. This simulation is virtually identical to our control case, $0X$, which is a 10 year simulation using one year of climatological monthly mean SSTs that are repeated each year. Fig. 13 of KHH compares the top-of-atmosphere, zonally averaged, annual mean outgoing longwave radiation (OLR) and absorbed solar radiation (ASR) to ERBE data. The comparison is excellent at most latitudes. For reference, we show OLR and ASR in Fig. 3a for our control simulation.

In Fig. 3b we show the components of the surface energy budget for the control simulation. At the surface there are considerably larger uncertainties in the magnitude of vertical energy fluxes that are available from observational datasets. KHH limit their discussion to the ocean surface and compare the model output to the dataset generated by Large et al. (1997), which is the one that is used to force the NCAR ocean model. The largest component of the net surface energy flux is the incoming shortwave radiation (dotted curve in Fig. 3b). Compared to the aforementioned dataset, the model tends to overestimate this component in the tropics by as much as 30 W m^{-2}, which is still within observational uncertainty. The latent heat flux is the other large component of the surface budget (dash-dotted in Fig. 3b). The low-latitude minimum is captured by the model, but the flux is underestimated by 10–20 W m^{-2} in the Northern Hemisphere (NH) and overestimated by about the same amount in the Southern Hemisphere (SH). The long-wave radiative flux (dashed in Fig. 3b), which is quite uncertain in the observational data, is overestimated by as much as 20 W m^{-2} in the subtropics. The smallest surface energy flux is that due to sensible heat (long dashes in Fig. 3b) and it tends to be overestimated in the model at low latitudes of the NH and at most latitudes in the SH. The net surface energy budget of the control simulation is shown by the solid curve in Fig. 3b. KHH found that the *net* surface energy budget showed remarkable agreement with observations (see their Fig. 12). This, of course, is one of the requirements for being able to couple the atmospheric and oceanic models without flux adjustments.

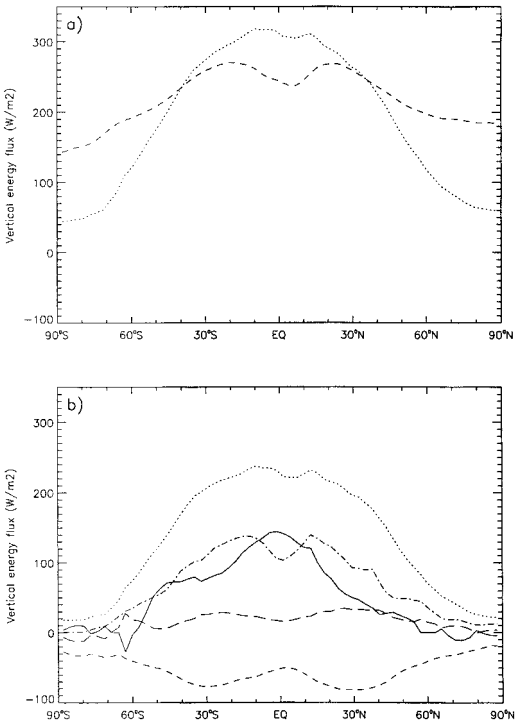

Fig. 3. Zonally averaged, annual-mean vertical energy flux (W m^{-2}) averaged over ten years of the control case ($0X$) as a function of latitude. (a) At the top of the atmosphere OLR (dashed) and ASR (dotted). (b) At the surface downward shortwave radiation (SWF, dotted), latent heat flux (LHF, dot-dashed), downward longwave radiation (LWF, dashed), sensible heat flux (SHF, long dashes), net downward surface energy flux (solid).

In Section 2, we showed that the divergence of the annual mean implied oceanic heat transport is equal to the annual mean net surface energy flux. Therefore, it is of primary importance that the model simulate these fluxes accurately. Fig. 14 of KHH shows the annual mean implied oceanic flux as simulated by CCM3, and as computed by

Trenberth and Solomon (1994) using atmospheric ECMWF analysis from 1988 combined with ERBE top-of-atmosphere radiation measurements for the same year (thus avoiding use of the much more uncertain surface energy estimates). The agreement is quite good in the NH, but gets poorer in low latitudes and in the SH where the model shows a maximum poleward transport that is about 1 PW ($1 \cdot 10^{15}$ W) less than the Trenberth and Solomon estimate at 15°S. In the context of the Trenberth and Solomon study, one should keep in mind that atmospheric observations are the poorest and scantest in this area. Therefore, their estimate of the implied oceanic heat transport is the least accurate in this region. In the study by Keith (1995), the poleward implied oceanic heat transport has a SH maximum at 40°S of 1.3 PW, however the error is estimated at ± 1 PW. This goes to illustrate the degree of uncertainty in the observational estimates of the implied ocean heat transport. As of yet only isolated direct measurements of oceanic heat transport are available. The two direct measurements discussed by Keith (1995) fall within the range of estimated error in the calculation.

Both observational studies quoted above implicitly assume that interannual variability is negligible. The Trenberth and Solomon (1994) study in that they only consider one year of data, that of 1988, and the Keith (1995) study in that the ERBE data is for different years (1985–1988) than the atmospheric analysis (1992–1993).

We evaluate the annual-mean, vertically integrated, meridional heat transport in the atmosphere, $\overline{[T_A]}$, by integrating the net energy flux at the top of the atmosphere and at the surface according to (2.3). The total (atmosphere and ocean) and the implied oceanic heat transport are computed similarly (by integrating the top-of-atmosphere net flux and the net surface flux, respectively), as described in Subsection 2.2. Fig. 4 shows some important features of the meridional heat transport. Fig. 4a shows the average total heat transport over the ten years of simulation, as well as the total transport in two extreme years, year 4 (dot-dashed) and year 6 (dashed). The standard deviation of the mean is 1% on average, so that interannual variability is negligible. Fig. 4b similarly shows the atmospheric heat transport, and Fig. 4c shows the (implied) oceanic heat transport averaged over ten years of the $0X$ simulation

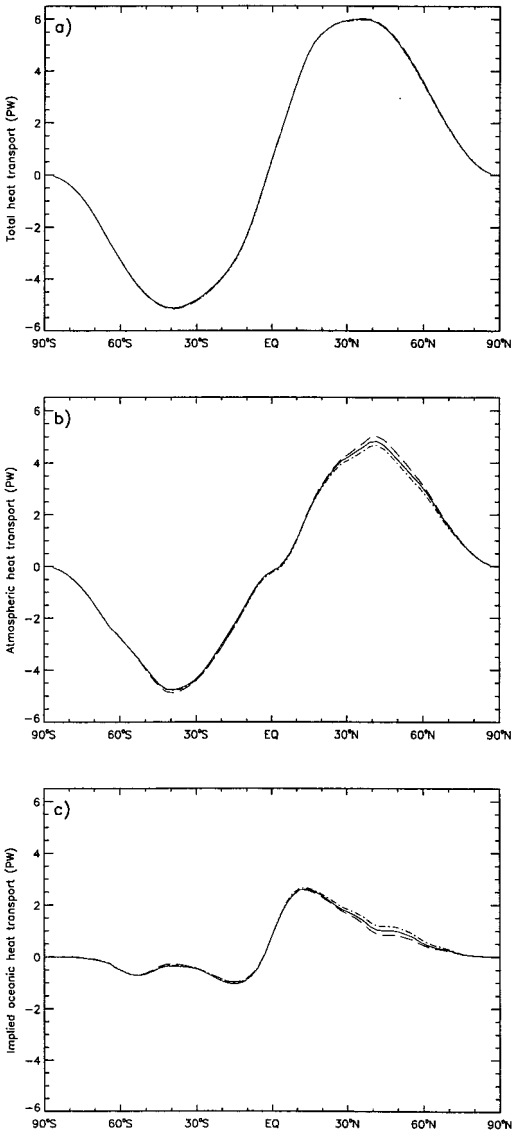

Fig. 4. Annual-mean, meridional heat transport (in PW) for the control case ($0X$) averaged over the ten years of simulation. Two extreme years are also included. year 4 (dot-dashed) and year 6 (dashed). (a) Total heat transport. (b) Atmospheric heat transport. (c) Implied oceanic heat transport.

with the two extreme years indicated as before. The standard deviation of the mean atmospheric heat transport is 4% on average and 19% for the mean (implied) oceanic heat transport. In Fig. 4 one can already detect some indication of the

compensating behaviour between atmosphere and ocean that will be discussed at length later. If we concentrate on midlatitudes in the NH, according to Fig. 4c the implied oceanic heat transport is relatively less in year 6 and relatively more in year 4. If we compare this to Fig. 4b and the atmospheric heat transport, we see that in midlatitudes in the NH the atmosphere transports less heat than usual in year 4 and more than usual in year 6. The end result is that interannual varibility is significantly less in the total heat transport than in any one of its two components. In other words, variability in the atmospheric heat transport is more closely tied to surface heat-flux variability, than to changes in the radiative fluxes at the top of the atmosphere.

In Subsections 3.2 and 3.3, where we discuss runs with different SST gradients, we show annual averages over nine years and we shall present the results as deviations from the $0X$ case.

3.2. *Meridional heat transport*

Fig. 5 shows results of annual-mean heat transport for the different cases ($1X$, $-5X$, $5X$, $9X$), shown as deviations from the control. The deviations of the mean (implied) oceanic heat transport from the control are shown in Fig. 5a. There are considerable differences between the different cases and at most latitudes, so that even though SSTs are changed the most in particular latitude bands, it influences the implied oceanic transport globally. Note that the $-5X$ signal (increased SST gradient) tends to be out of phase with the other cases (all of which have decreased SST gradient compared to the control).

The deviations of the atmospheric heat transport depicted in Fig. 5b show considerably less variability, relatively speaking, than those for the implied oceanic transport. Note that there is a certain element of compensation in that the deviations of the total transport shown in Fig. 5c generally exhibit less variability between cases than either the atmosphere or the ocean separately. It appears that the atmosphere is trying to compensate for the change in implied oceanic heat transport so as to make the total annual-mean heat transport vary less than either of its components. The only exception to this behaviour is the $-5X$ case, where the total transport (Fig. 5c) in the SH is greater than for any of the other cases.

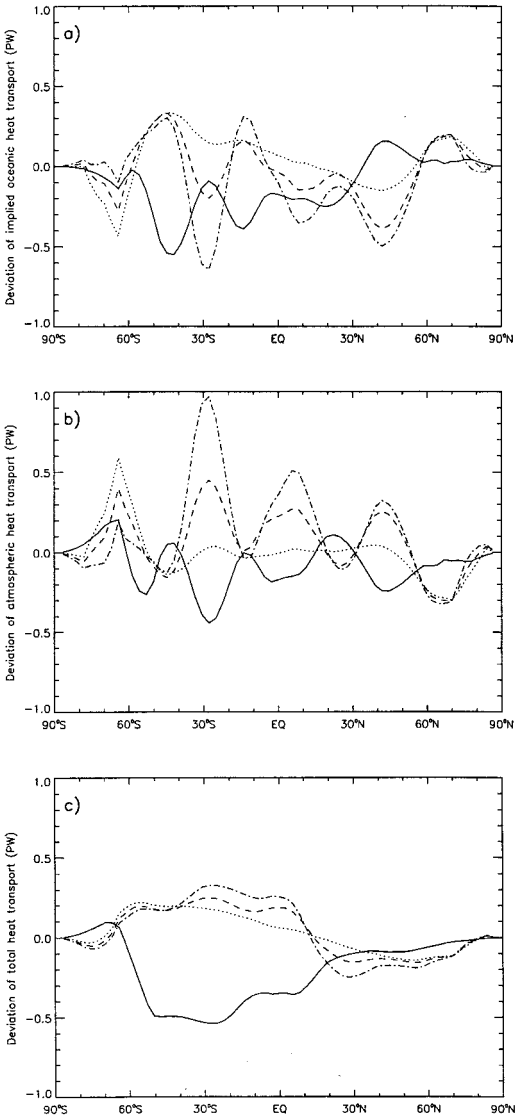

Fig. 5. Annual-mean, meridional heat transport (in PW) averaged over nine years for the different experiments, shown as deviations from the control case. $-5X$ (solid), $1X$ (dotted), $5X$ (dashed), $9X$ (dot-dashed). (a) Implied oceanic heat transport deviations. (b) Atmospheric heat transport deviations. (c) Total heat transport deviations.

Note that both components of the deviation in $-5X$ transport, the atmospheric component in Fig. 5b and especially the implied oceanic heat transport in Fig. 5a, are considerably greater for the $-5X$ case than for any of the other cases.

We can examine the transport of moist static energy in the atmosphere by separating it into the transport of dry static energy and the transport of latent heat. Fig. 6a shows this decomposition for year 3 of the control simulation. Of note in Fig. 6a is the great deal of cancellation at low latitudes between latent heat transport (dotted) and dry static energy transport (dashed) associated with the Hadley circulation. The dry static energy transport is directed poleward because the equatorial region is warmer than the subtropics. However, the maximum evaporation tends to take place off the equator since the annual-mean ITCZ with its associated precipitation maximum is located at equatorial latitudes. Hence the latent heat transport tends to be of opposite sign to the dry static energy transport. The deviation from the control for each of the four cases is shown in Fig. 6b for latent heat transport and in Fig. 6c for dry static energy transport. The tendency in each case for the deviations of these two components to cancel is particularly noticeable when comparing Figs. 6b and 6c. The exception to this cancellation behaviour is in the subtropics where the signal is small. By far the largest contribution to the deviation in both components of atmospheric heat transport for $5X$ and $9X$ is at low latitudes corresponding to a more intense Hadley circulation. The annual-mean Hadley circulation also appears to become symmetrical with respect to the equator for these two cases. As before, the two components of energy transport tend to cancel. For $1X$ and $-5X$, dry static energy is the more important contribution to atmospheric heat transport.

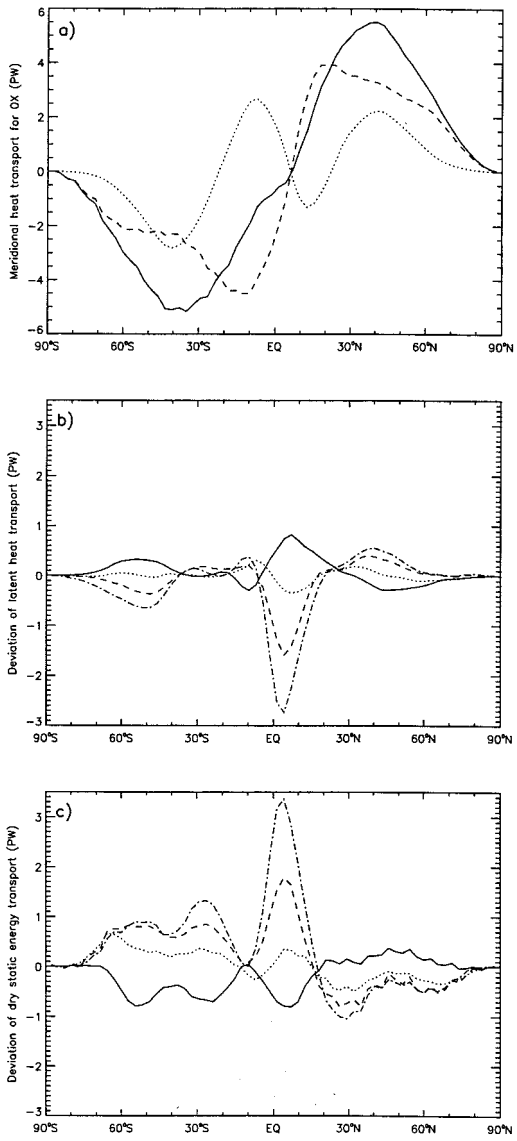

Fig. 6. (a) Meridional transport (in PW) of moist static energy (solid), dry static energy (dashed) and latent heat (dotted) for the annual mean of year 3 of the control case ($0X$). (b) Deviations from $0X$ of meridional latent heat transport for the year-3, annual mean, $-5X$ (solid), $1X$ (dotted), $5X$ (dashed), $9X$ (dot-dashed). (c) Same as (b) except deviations from $0X$ of dry static energy transport.

Thus, both components of the atmospheric heat transport seem to be contributing to the change in total atmospheric heat transport, which tends to oppose changes in oceanic heat transport. In midlatitudes, we see from Fig. 6b that as we go from $-5X$ to the cases with warmer SSTs (see Table 1) the poleward transport of latent heat increases. As the SSTs warm so do the lower tropospheric temperatures and as a result the atmosphere can hold more water vapour. One would therefore expect that the eddies carry more latent heat. At the same time, we see from Fig. 6c that the poleward transport of dry static energy tends to decrease as we go to the cases with warmer SSTs in midlatitudes. However, the warmer cases are also the cases where the high-latitude SST gradient has been substantially decreased. Hence we expect the transient eddies to carry less dry static energy.

Manabe and Bryan (1985) found that atmo-

spheric heat transport did not vary significantly between cases that had widely different CO_2 concentrations. In their coupled GCM integrations the oceanic transport did not change much between experiments. The two components of the atmospheric heat transport changed such that the total atmospheric heat transport did not vary much between experiments. Thus they concluded that there is a certain compensation between the change in dry static energy transport and the change in latent heat transport. Our results above confirm their conclusions.

3.3. *Vertical energy fluxes at the top of the atmosphere and at the surface*

The CCM3 conserves energy to a high degree of accuracy (KHH). The global, top-of-atmosphere model fluxes are tuned to agree with ERBE data for climatological SSTs. As we have already discussed, there is, however, considerable uncertainty in the individual, vertical, surface energy fluxes in the model. Here we consider the annual and zonal average of the vertical energy fluxes for the different model experiments, represented as deviations from the control simulation.

Fig. 7 shows the deviation of the top-of-atmosphere radiative fluxes from the control as a function of latitude, OLR in Fig. 7a and ASR in Fig. 7b. There are significant changes in OLR between cases, such that going from the coolest SSTs (corresponding to $-5X$) to the warmest SSTs (corresponding to $9X$) there is a steady increase in OLR at all latitudes except in a latitude band stretching from the equator to about 10°S. Note that the change in OLR is not linearly dependent on the change in SST (Fig. 1) as simple empirical formulae would predict (e.g., Budyko, 1969). The sign of OLR change is in the same sense as the sign of SST change, but the constant of proportionality is latitude dependent. The high-latitude changes in ASR are quite substantial, but since they are for the most part associated with the way in which the atmospheric model somewhat arbitrarily decides on an ice edge, they are not very physical.

In fact, the deviations in ASR for the different cases are most interesting at low latitudes. These are associated with changes in tropical cloudiness, signatures of which are also seen in the changes in OLR. For example, for the $9X$ case, OLR has

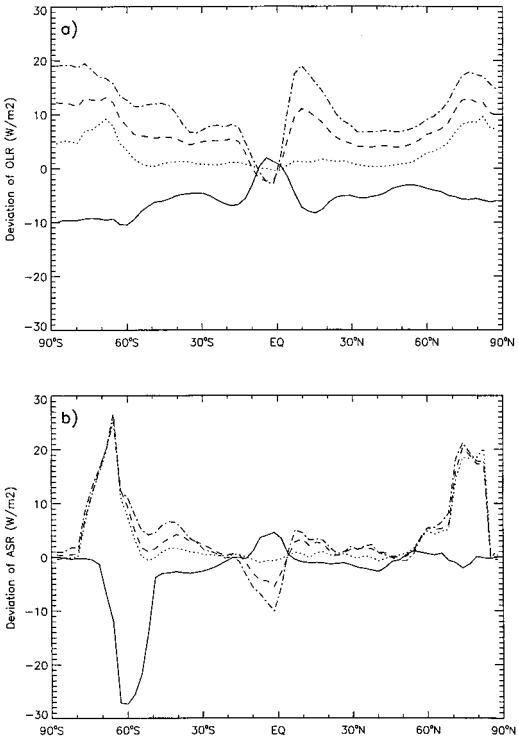

Fig. 7. Zonally averaged, annual-mean, vertical energy flux (W m^{-2}) at the top of the atmosphere averaged over nine years, shown as deviations from the control case ($0X$), as functions of latitude. $-5X$ (solid), $1X$ (dotted), $5X$ (dashed), $9X$ (dot-dashed). (a) Deviations of OLR from $0X$. (b) Deviations of ASR from $0X$.

actually decreased a little (signifying cooler cloud tops or increased cloudiness) in equatorial latitudes and ASR has decreased significantly. In the tropics, changes in SST have a greater effect on ASR than on OLR. The OLR response to warmer SSTs is affected by the water vapour greenhouse effect that provides a weak positive feedback by trapping heat within the atmosphere. However, the ASR response provides a stronger, negative feedback because less heat is absorbed. The increase in LHF that is seen in the surface budget (Fig. 8c) would also be consistent with increased convection and cloudiness in the tropics.

Fig. 8 shows the annual and zonal average of components of the surface energy budget as deviations from the control. The deviations in net downward longwave radiation (LWF) at the surface for the different cases are shown in Fig. 8a. Outside of

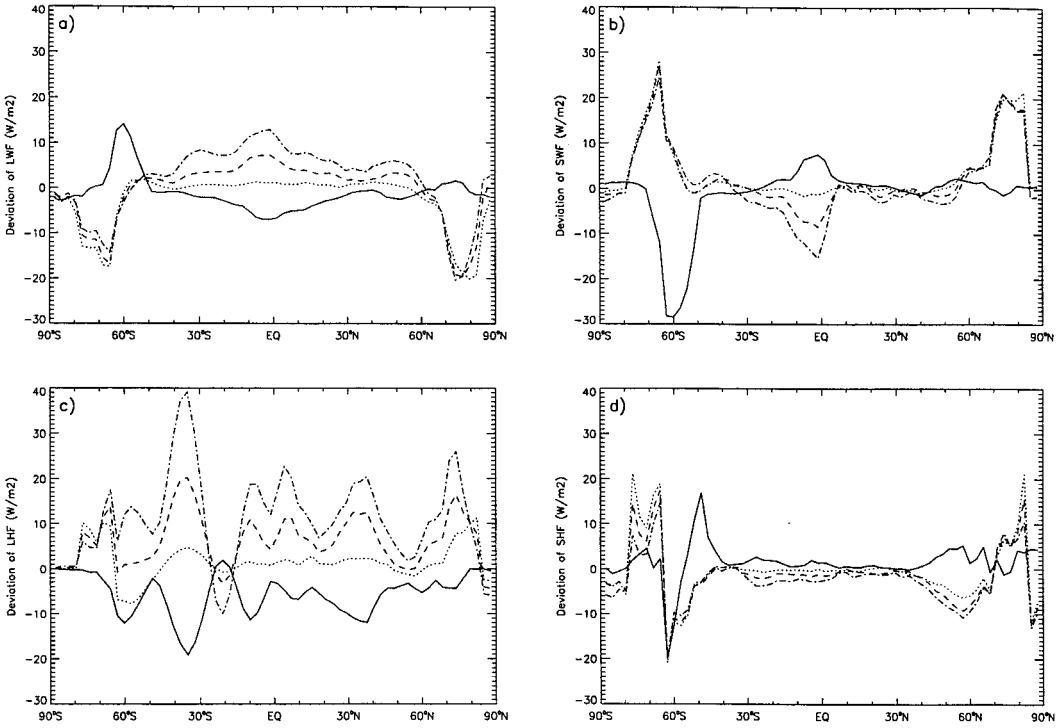

Fig. 8. Same as Fig. 7 except for vertical energy flux at the surface. (a) Deviations of downward longwave radiation (LWF) from $0X$. (b) Deviations of downward shortwave radiation (SWF) from $0X$. (c) Deviations of the latent heat flux (LHF) from $0X$. (d) Deviations of the sensible heat flux (SHF) from $0X$.

high latitudes, the deviations in LWF are positive when the SST is increased, and they are more positive the larger the increase in SST. The LWF is determined by a combination of several factors, including surface temperature and longwave opacity, which is related to the greenhouse effect. The deviations in downward shortwave radiation (SWF) shown in Fig. 8b are very close to the deviations in top-of-atmosphere ASR shown in Fig. 7b. Thus, the changes in the shortwave budget at the top-of-the-atmosphere are seen pretty much unmodified at the surface. This is not surprising, since the atmosphere does not absorb much shortwave radiation, as parameterized in CCM3. Note, however, that some researchers claim that there is significant shortwave absorption in the atmosphere (e.g., Ramanathan et al., 1995).

The other components of the surface energy budget are shown in Fig. 8c (latent heat flux, LHF) and Fig. 8d (sensible heat flux, SHF), represented as deviations from the control. At most latitudes the $9X$ case has the most positive deviation of LHF from the control, followed by $5X$ and $1X$, whereas $-5X$ has a negative deviation of LHF at most latitudes. This is not unexpected because of the strong dependence of saturation water vapour pressure on temperature. Perhaps the meridional structure is of most interest (especially for the $9X$ case) showing minimal deviations from the control that are most pronounced around 20°S where all the cases seem to converge. There is a secondary minimum in LHF deviations at 55°N. The SHF deviations in Fig. 8d also show meridional structure with a stronger signal of deviations at 55°N for all four cases.

4. Winter-mean budgets

The midlatitude eddies get particularly vigorous during the winter season of each hemisphere. It is of interest to examine the separate contributions

to the heat transport, from eddies on the one hand and from the mean meridional circulation on the other hand. The eddy heat transport can then be further devided into a contribution due to transient eddies and a contribution due to stationary eddies. The transients owe their existence to baroclinic instability whereas the stationary eddies depend on surface zonal inhomogeneties. Because of the uneven distribution of continents and ocean between the two hemispheres, the stationary waves are also different. The NH supports far more stationary eddy activity than the SH, and most global warming scenarios tend to exaggerate this behaviour. This is directly related to the fact that the surface warming that occurs tends to take place primarily over land, leading to further temperature contrasts between land and ocean and more stationary wave activity. We shall briefly return to this issue in Section 5.

If we denote the moist static energy density ($c_p\,T + gz + Lq$) by ε, the seasonal and zonal mean of the meridional energy transport when separating the different terms becomes

$$\overline{[\varepsilon v]} = [\bar{\varepsilon}][\bar{v}] + \overline{[\varepsilon' v']} + [\bar{\varepsilon}^* \bar{v}^*], \tag{4.1}$$

where the 1st term on the right-hand side represents the heat transport by the mean meridional circulation, the second term the transport by transient eddies and the last term the transport due to stationary eddies. The square brackets represent a zonal average, the star a deviation from the zonal average, the overbar a time mean over the three months (DJF or JJA) of all 10 years of simulation, and the prime a deviation from the time mean. As discussed by Keith (1995), when using (4.1) in vertical coordinates other than pure pressure coordinates, such as the hybrid pressure-sigma coordinates used in CCM3, the appropriate zonal average to use is the mass-weighted zonal average. The instantaneous atmospheric model data was saved twice per day.

One further decomposition of the meridional, moist static energy transport that we have already discussed for the annual-mean case is the relative contribution of dry static energy ($c_p T + gz$) transport compared to latent heat (Lq) transport. In each case, we shall restrict the discussion to the winter hemisphere.

4.1. *Northern hemisphere winter (DJF)*

Let us first examine the control case. Then we shall discuss the other cases as deviations from the control. In Fig. 9 we decompose the moist static energy transport of $0X$ (solid) into components corresponding to the mean meridional transport (dashed), stationary eddy transport (dash-dotted) and transient eddy transport (dotted), according to (4.1) for DJF. The eddies are by far the most effective carriers of energy to the poles, and the transients are far more effective than the stationary eddies. There is a great deal of cancellation in the mean meridional transport of moist static energy at low latitudes, between transports of dry static energy and latent heat. The large negative mean meridional latent heat transport associated with the Hadley Cell is by far the largest component to the latent heat transport. The components associated with eddy transport of latent heat are minor by comparison and directed poleward. Outside of low latitudes, the transients are the largest contributor to both dry static energy and latent heat transport.

The decomposition (according to (4.1)) of the DJF moist static energy transport was calculated for each of the perturbed cases ($1X$, $5X$, $-5X$, $9X$). Results (as deviations from the control) are shown in Figs. 10a–d: total transport, mean meridional transport, transient eddy transport and stationary eddy transport, respectively.

Let us concentrate on the NH. Note that the dominance of stationary eddy contributions (Fig. 10d) in the deviations is quite different from the control-case partition (Fig. 9), where the transient eddy contribution dominates. There is an increase in $9X$ and $5X$ total heat transport at

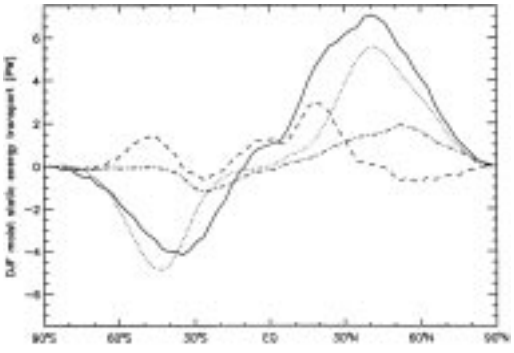

Fig. 9. DJF-mean moist static energy transport (solid), averaged over ten years for the control case (in PW); decomposed into mean-meridional part (dashed), stationary-eddy part (dot-dashed) and transient-eddy part (dotted).

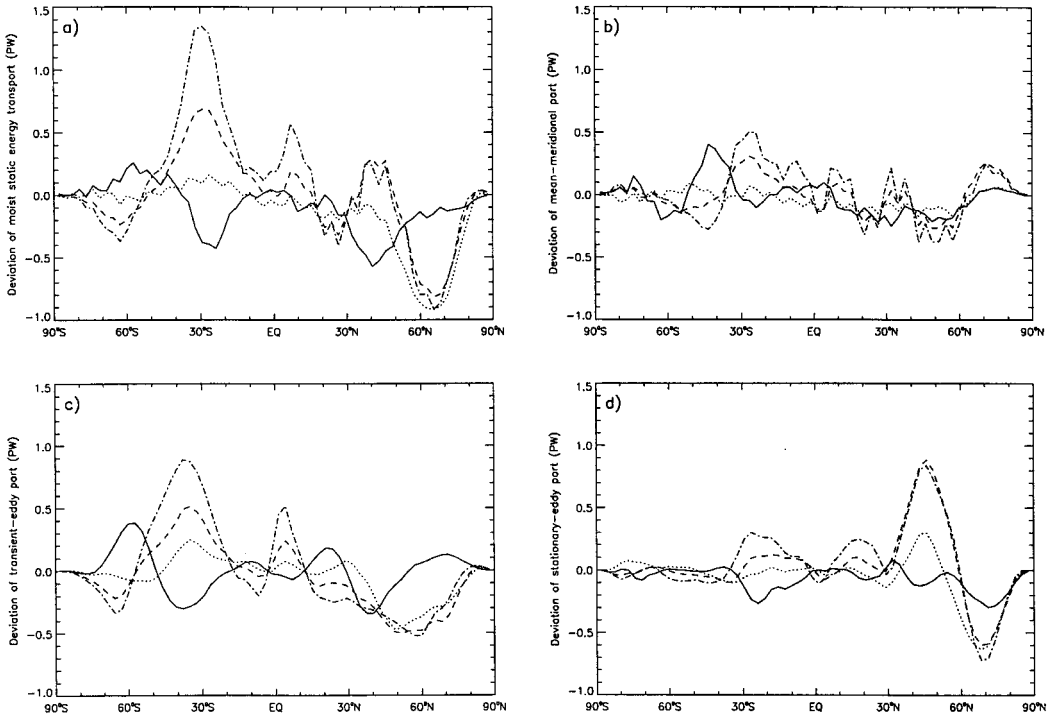

Fig. 10. DJF-mean deviations of the moist static energy components (in PW) of $-5X$ (solid), $1X$ (dotted), $5X$ (dashed), $9X$ (dot-dashed) from the control case $0X$. (a) Total moist static energy transport deviations. (b) Mean-meridional part of the moist static energy transport deviations. (c) Transient-eddy part of the moist static energy transport deviations. (d) Stationary-eddy part of the moist static energy transport deviations.

midlatitudes that is primarily the result of a very significant increase in stationary eddy transport that is partially cancelled by a decrease in poleward transient transport. Since the SST gradient has been decreased for these two cases, the decrease in transient transport is to be expected. The behaviour of the stationary waves may seem counterintuitive at first, but keep in mind that for the winter hemisphere when the SST gradient is decreased (and SSTs warmed fairly uniformly south of 50°N according to Fig. 1), there is more of a contrast between the cold continents and the relatively warm ocean. Such temperature contrast will support increased activity of stationary waves. North of about 50°N the negative change in transient transport is reinforced by a negative change in stationary transport and there is a sharp decrease in the total transport for the two cases. It seems that the stationary eddy transport is sensitive to the actual SST value and its gradient, whereas the transient eddy transport depends only on the gradient.

4.2. *Southern hemisphere winter (JJA)*

In Fig. 11, we decompose the moist static energy transport of $0X$ (solid) into components corresponding to the mean meridional transport (dashed), stationary eddy transport (dash-dotted) and transient eddy transport (dotted), according to (4.1) for JJA. The transients clearly dominate the SH heat transport. The transport accomplished by stationary waves is negligible in the SH. This is because the SH is dominated by an ocean surface that does not support the zonal inhomogeneities that the stationary waves require.

We further split the moist static energy transport into components corresponding to latent heat and dry static energy transport. As before, there is a great deal of cancellation between the low-latitude

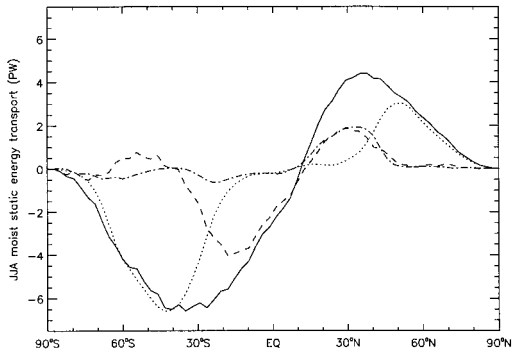

Fig. 11. Same as Fig. 9 except for JJA mean.

latent heat and dry static energy transport. Outside of low latitudes the dry static energy transport dominates compared to latent heat.

Fig. 12 shows results for SH winter for the different cases ($1X$, $5X$, $-5X$, $9X$), shown as deviations from the $0X$ case in Fig. 11. We depict the deviations for total moist static energy in Fig. 11a, for the mean meridional transport in Fig. 11b, for the transients in Fig. 11c and for the stationaries in Fig. 11d. There is a marked increase in poleward total heat transport in the SH for the $-5X$ case. At midlatitudes this increase is due to a significant increase of transient transport, but at lower latitudes it is due to the mean meridional circulation. It is of interest that this increase in moist static energy transport by the mean meridional circulation is not matched by a change in latent heat transport by the mean meridional circulation (not shown). Thus it is primarily due to a change in dry static energy transport. The cases where the SST gradient is decreased show a decrease in poleward transient transport that is the most noticeable for the $9X$ case.

5. Concluding remarks

The picture that emerges from our numerical experiments is one of remarkable compensation between changes in (implied) ocean heat transport and variability in atmospheric heat transport. It is almost as if one could place an insulating lid at the top of the atmosphere as far as small climate

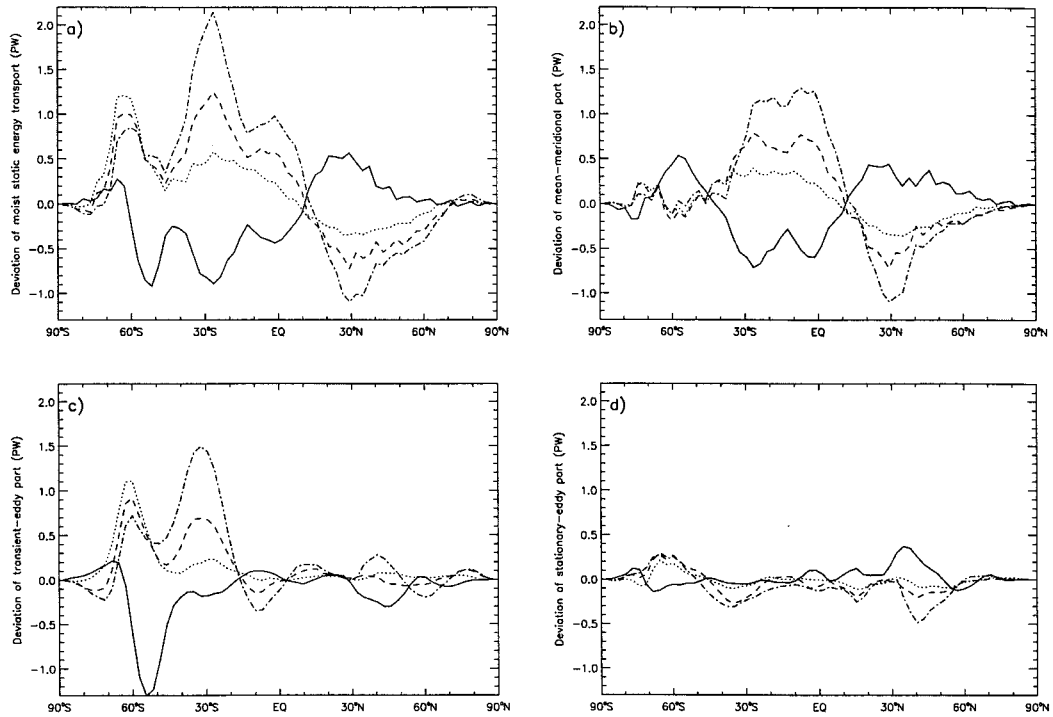

Fig. 12. Same as Fig. 10 except for JJA mean.

perturbations are concerned. Below the lid there may be different partitionings in heat transport between the atmosphere and ocean, but the combined heat transport in the climate system is remarkably constant. This compensating behaviour contributes to the stability of climate. One might speculate that in the event of the complete shutdown of the thermohaline circulation, the atmospheric heat transport would increase sufficiently to make up for the lack of oceanic transport. Certainly, simple coupled climate models (e.g., Saravanan and McWilliams, 1995) predict that this is indeed the case.

We attribute the high level of compensation at least in part to the high dynamical efficiency of atmospheric eddy transport. The atmospheric eddies are extremely efficient at redistributing heat horizontally. The one-dimensional, energy-balance models that we discussed in the first section, estimate the dynamical efficiency as a diffusion coefficient (e.g., North, 1975; Lorenz, 1979). We might take a similar approach in order to define an estimate of dynamical efficiency. A natural quantity to consider is the net zonally averaged energy that is absorbed in the atmosphere per unit time and per unit area, let us call it F_{atm}. In our previous notation, $F_{\mathrm{atm}} = \mathrm{LHF} + \mathrm{SHF} - F_{\mathrm{S}} - F_{\mathrm{T}}$, it is the net vertical, zonally-averaged energy flux entering the atmosphere at the surface minus the net vertical, zonally averaged energy flux leaving the top of the atmosphere. Now, this quantity will be redistributed horizontally in the atmosphere, and to a first approximation we can assume that the resulting heat flux is proportional to the gradient of the zonally averaged surface temperature, T_{sfc}, or

$$F_{\mathrm{atm}} = \nabla \cdot (\nu \nabla T_{\mathrm{sfc}}). \tag{5.1}$$

If we assume that ν, the diffusion coefficient, is constant, then the net energy flux into the atmosphere is equal to a constant times the Laplacian of zonally-averaged surface temperature.

We have the means of testing the above relation (5.1) in our numerical experiments. Since the parameter we vary between experiments is the zonally averaged SST, it is natural to express (5.1) in terms of the Laplacian of zonally averaged SST. Fig. 13 shows a scatterplot of the difference between net, zonally averaged, vertical flux into the atmosphere (F_{atm}) normalized by the trend-factor (column 1, Table 1), and the control, as a function of the

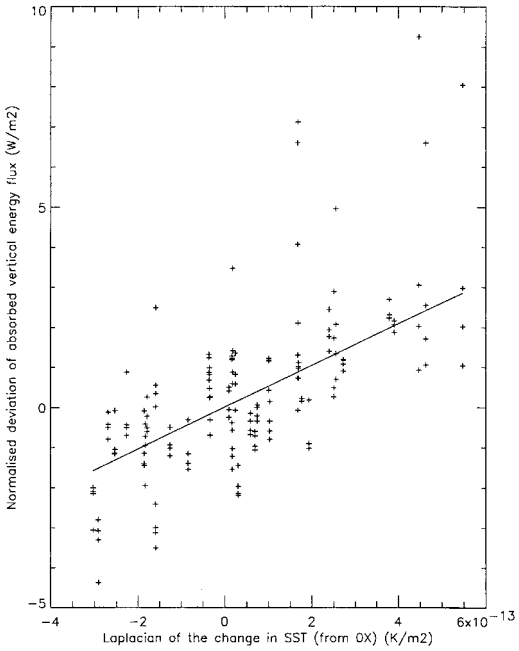

Fig. 13. Scatterplot representing all the perturbation experiments, latitudes from 50° S to 60° N, of the deviation from the control of the net zonally averaged, vertical energy flux absorbed in the atmosphere (F_{atm}), scaled by the trend-factor, (W m^{-2}) as a function of the Laplacian of the change in SST for all experiments and latitudes from 50° S to 60° N (in Km^{-2}).

Laplacian of the change in SST (∇^2SSTtrend) for all experiments and latitudes from 50°S to 60°N. Fig. 13 indicates an approximately linear relation between F_{atm} and ∇^2SSTtrend, implying a weaker sensitivity to the meridional temperature gradient than that predicted by most atmospheric eddy flux parameterization schemes. All the "outliers" in the figure correspond to high-latitude locations. We fitted the data by a line using a "robust" least absolute deviation method (e.g., Press et al., 1989, Subsection 14.6). The resulting slope has the value $5.3 \cdot 10^{12}$ W K^{-1}, which is quite close to other empirical estimates such as the value $\nu = 8 \cdot 10^{12}$ W K^{-1} used by Rahmstorf and Willebrand (1995).

The diffusive approximation for atmospheric heat transport may be valid in a gross sense but not in detail, as indicated by the significant scatter in Fig. 13. Although the proportionality between the meridional heat flux and the meridional temperature gradient assumed in (5.1) may be valid

for transient eddies, it is not clear that it applies to stationary eddies. The stationary-eddy transport would depend on the zonal temperature inhomogeneties as well as the meridional gradient. The rôle of zonal temperature inhomogeneties is neglected in the zonally averaged diffusive parameterizations for the meridional heat flux. In our experiments, we saw that as the SSTs were increased ($5X$, $9X$) in DJF, the heat transported by NH, wintertime, stationary eddies increased significantly south of 50°N. At those latitudes the increase in SST is relatively uniform leading to an increased temperature contrast between land and ocean, and increased stationary-wave heat transport. The heat transport associated with the transient waves, however, decreased in the same latitudes.

At the top of the atmosphere, the radiative flux is affected in an interesting way by the change in tropical SST. This change corresponds to an increase in cloudiness as the SST is warmed. The shortwave component (ASR) shows a strong negative feedback. As the SST is increased there is increased cloudiness and higher planetary albedo. The longwave component (OLR) shows a weak positive feedback, corresponding to an increase in the concentration of water vapour as well as increased cloud amounts that would lead to increased greenhouse effect. This negative shortwave feedback on the SST in the tropics is quite distinct from the negative longwave feedback on the SST that dominates the extratropics. This suggests that the atmospheric radiative and convective processes, as parameterized in CCM3, tend to counteract changes in zonal-mean tropical SST. This is reminiscent of the thermodynamic regulation proposed by Ramanathan and Collins (1991) in a different context.

In our discussion we have emphasised the two warm SST cases, experiments $5X$ and $9X$. These two cases are somewhat like scenarios for global warming, except that the atmospheric composition has not been explicitly changed and oceanic properties such as SSTs are prescribed. Note that some greenhouse gas changes affect the vertical structure of the atmosphere, which is not considered here. Another very important effect of changing the atmospheric composition is to increase the land-surface temperatures directly through radiation. In the $5X$ and $9X$ cases, the increase in land surface temperature occurs only because of the SST change and the associated changes in atmospheric moisture. Referring back to Table 1, we see that even without explicitly changing the atmospheric conditions over land, the temperature increase over land is greater than the globally averaged temperature increase. This implies that the direct effects of changing atmospheric composition and thereby changing the radiation may be far less important than the indirect effects of a changed moisture content. It also implies that many of our conclusions regarding atmospheric heat transport would continue to be valid for cases where the change in SST is associated with a change in the atmospheric composition, such as the global warming scenarios. In particular, we should expect to see a redistribution of the atmospheric heat transport between the the latent heat and dry static energy components, if the global warming trend continues. We should also expect to see much greater heat flux variability at the surface than at the top of the atmosphere, associated with the atmospheric compensation for changes in the (implied) oceanic heat transport.

6. Acknowledgments

The authors wish to thank Didi Sariyska for assistance with the data analysis and two anonymous referees for helpful comments on the manuscript. This work was supported by the National Science Foundation under grant ATM-9615864. Allocations of computer time were made by the San Diego Supercomputer Center and the Scientific Computing Division of NCAR.

REFERENCES

Broecker, W. S., D. M. Peteet and D. Rind, 1985. Does the ocean–atmosphere have more than one stable mode of operation? *Nature* **315**, 21–26.

Bryan, F. 1986. High latitude salinity effects and interhemispheric circulations. *Nature* **323**, 21–25.

Budyko, M. I. 1969. The effect of solar radiation variations on the climate of the Earth. *Tellus* **21**, 611–619.

Carissimo, B. C., A. H. Oort and T. H. VonderHaar, 1985. Estimating the meridional energy tranports in the atmosphere and ocean. *J. Phys. Ocean.* **15**, 82–91.

Green, J. S. A. 1970. Transfer properties of the large-scale eddies and the general circulation of the atmosphere. *Q. J. Roy. Meteorol. Soc.* **96**, 157–185.

IPCC, 1996. *Climate change 1995: The science of climate change*. J. T. Houghton, L. G. Meira Filho, B. A. Callander, N. Harris, A. Kattenberg and K. Maskell (eds). Cambridge University Press, 572 pp.

Kasahara, A. 1974. Various coordinate systems used for numerical weather prediction. *Mon. Wea. Rev.* **102**, 509–522.

Kerr, R. A. 1995. Climate modeling's fudge factor comes under fire. *Science* **265**, 1528.

Keith, D. W. 1995. Meridional energy transport. uncertainty in zonal means. *Tellus* **47A**, 30–44.

Kiehl, J. T., J. J. Hack, G. B. Bonan, B. A. Boville, B. P. Briegleb, D. J. Williamson and P. J. Rasch, 1996. *Description of the NCAR Community Climate Model (CCM3)*. NCAR Technical Note, September 1996, 152 pp.

Kiehl, J. T., J. J. Hack, G. B. Bonan, B. A. Boville, D. L. Williamson and P. J. Rasch, 1998a. The National Center for Atmospheric Research community climate model: CCM3. *J. Climate* **11**, 1131–1149.

Kiehl, J. T., J. J. Hack and J. W. Hurrell, 1998b. The energy budget of the NCAR community climate model: CCM3. *J. Climate* **11**, 1151–1178.

Large, W. G., G. Danabasoglu, S. C. Doney and J. C. McWilliams, 1997. Sensitivity to surface forcing and boundary layer mixing in a global ocean model. *J. Phys. Oceanogr.* **27**, 2418–2447.

Lorenz, E. N. 1979. Forced and free variations of weather and climate. *J. Atmos. Sci.* **36**, 1367–1376.

Manabe, S. and K. Bryan, 1985. CO_2-induced change in a coupled ocean–atmosphere model and its paleoclimatic implications. *J. Geophys. Res.* **90**, 11689–11707.

Manabe, S. and R. J. Stouffer, 1988. Two stable equilibria of a coupled ocean–atmosphere model. *J. Climate* **1**, 841–866.

North, G. R. 1975. Theory of energy-balance models. *J. Atmos. Sci.* **32**, 2033–2043.

Press, W. H., B. P. Flannery, S. A. Teukolsky and W. T. Vetterling, 1989. *Numerical recipes, the art of scientific computing*. Cambridge University Press, 818 pp.

Rahmstorf, S. and J. Willebrand, 1995. The rôle of temperature feedback in stabilizing the thermohaline circulation. *J. Phys. Oceanogr.* **25**, 787–805.

Ramanathan, V. and W. Collins, 1991. Thermodynamic regulation of ocean warming by cirrus clouds deduced from observations of 1987 El Nino. *Nature* **351**, 27–32.

Ramanathan, V., B. Subasilar, G. J. Zhang, W. Conant, R. D. Cess, J. T. Kiehl, H. Grassl and L. Shi, 1995. Warm pool heat budget and shortwave cloud forcing: a missing physics? *Science* **267**, 499–503.

Rayner, N. A., Folland, C. K., Parker, D. E., Horton, E. B. 1995. A new global sea-ice and sea surface temperature (GISST) data set for 1903–1994 for forcing climate models. Hadley Centre Internal Note No. **69**, 9 pp. (Available from the Hadley Centre, Meteorological Office, Bracknell, UK).

Saravanan, R. and J. C. McWilliams, 1995. Multiple equilibria, natural variability, and climate transitions in an idealized ocean–atmosphere model. *J. Climate* **8**, 2296–2323.

Stommel, H. 1961. Thermohaline convection with two stable regimes of flow. *Tellus* **13**, 224–230.

Stone, P. H. 1978. Constraints on dynamical transports of energy on a spherical planet. *Dyn. Atmos. Oceans* **2**, 123–139.

Stone, P. H. and L. Branscombe, 1992. Diabatically forced near inviscid eddy regimes. *J. Atmos. Sci.* **49**, 355–367.

Stone, P. H. and D. A. Miller, 1980. Empirical relations between seasonal changes in meridional temperature gradients and meridional fluxes of heat. *J. Atmos. Sci.* **37**, 1708–1721.

Trenberth, K. E., and A. Solomon, 1994. The global heat balance. heat transports in the atmosphere and ocean. *Clim. Dyn.* **10**, 107–134.

Zhang, Y-C. and W. B. Rossow, 1997. Estimating meridional energy transports by the atmospheric and oceanic general circulations using boundary fluxes. *J. Climate* **10**, 2358–2373.

Zhou, S. and P. H. Stone, 1993a. The rôle of large-scale eddies in the climate equilibrium. Part I: Fixed static stability. *J. Climate* **6**, 985–1001.

Zhou, S. and P. H. Stone, 1993b. The rôle of large-scale eddies in the climate equilibrium. Part II: Variable static stability. *J. Climate* **6**, 1871–1881.